Metalloporphyrin-Encapsulated Biodegradable Nanosystems for Highly Efficient Magnetic Resonance Imaging-Guided Sonodynamic Cancer Therapy

Ping Huang,[†,∥] Xiaoqin Qian,[§,∥] Yu Chen,*[‡] Luodan Yu,[‡] Han Lin,[‡] Liying Wang,[‡] Yufang Zhu,*[†] and Jianlin Shi*[‡]

[†]School of Materials Science and Engineering, University of Shanghai for Science and Technology, Shanghai 200093, P. R. China

[‡]State Key Laboratory of High Performance Ceramics and Superfine Microstructure, Shanghai Institute of Ceramics, Chinese Academy of Sciences, Shanghai 200050, P. R. China

[§]Department of Ultrasound, The Affiliated People's Hospital of Jiangsu University, Zhenjiang 212002, P. R. China

Ⓢ Supporting Information

ABSTRACT: Traditional photodynamic therapy (PDT) suffers from the critical issues of low tissue-penetrating depth of light and potential phototoxicity, which are expected to be solved by developing new dynamic therapy-based therapeutic modalities such as sonodynamic therapy (SDT). In this work, we report on the design/fabrication of a high-performance multifunctional nanoparticulate sonosensitizer for efficient *in vivo* magnetic resonance imaging (MRI)-guided SDT against cancer. The developed approach takes the structural and compositional features of mesoporous organosilica-based nanosystems for the fabrication of sonosensitizers with intriguing theranostic performance. The well-defined mesoporosity facilitates the high loading of organic sonosensitizers (protoporphyrin, PpIX) and further chelating of paramagnetic transitional metal Mn ions based on metalloporphyrin chemistry (MnPpIX). The mesoporous structure of large surface area also maximizes the accessibility of water molecules to the encapsulated paramagnetic Mn ions, endowing the composite sonosensitizers with markedly high MRI performance ($r_1 = 9.43$ mM^{-1} s^{-2}) for SDT guidance and monitoring. Importantly, the developed multifunctional sonosensitizers (HMONs-MnPpIX-PEG) with controllable biodegradation behavior and high biocompatibility show distinctively high SDT efficiency for inducing the cancer-cell death *in vitro* and suppressing the tumor growth *in vivo*. This report provides a paradigm that nanotechnology-enhanced SDT based on elaborately designed high-performance multifunctional sonosensitizers will pave a new way for efficient cancer treatment by fully taking the advantages (noninvasiveness, convenience, cost-effectiveness, etc.) of ultrasound therapy and quickly developing nanomedicine.
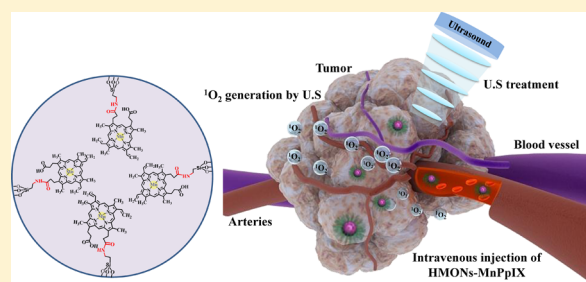
1. INTRODUCTION

Cancer is now one of the most serious diseases threatening the health of human beings.[1] The development of novel therapeutic modalities with concurrently high efficiency and mitigated side effects is of great significance in combating cancer.[2−5] One example, photodynamic therapy (PDT), employs light to activate photosensitizers to generate reactive oxygen species (ROS), which are highly toxic to cancer cells for suppressing tumor growth.[6−8] The relatively low-penetrating depth of light, however, severely restricts the further clinical translation of PDT, though near-infrared (NIR) has been developed to partially solve the depth issue of light in tissue.[9−12]

As a mechanical wave, ultrasound (US) has found broad biomedical applications, either in the form of diagnostic US imaging or US-based cancer therapy (e.g., high-intensity focused ultrasound).[13−15] It is highly intriguing that US could activate the sonosensitizers to generate ROS for inducing cancer-cell death.[16,17] This therapeutic modality is typically termed as sonodynamic therapy (SDT), in comparison to

conventional PDT.[18,19] The most important advantage of SDT is the high tissue-penetrating depth of US as the irradiation source compared to traditional light-triggered PDT. Similar to photosensitizers for PDT, various organic sonosensitizers have been adopted for SDT, including photofrin, hematoporphyrin, chlorophyll derivatives, phthalocyanine, etc.[20−22] However, these organic sonosensitizer molecules suffer from low chemical and biological stability, reluctant tumor-accumulation, and thereafter low SDT efficiency. Compared to organic sonosensitizers, inorganic sonosensitizers such as TiO$_2$ nanoparticles have also been demonstrated to be effective for SDT, owing to their unique energy-band structure and relatively high chemical/physiological stability, but biodegradation and biosafety issues are the main obstacles in their further clinical translation.[17,23−25]

Mesoporous silica nanoparticles (MSNs) have been extensively explored in biomedicine because of their well-defined mesoporous nanostructures with large surface area and high pore volume, which provide large reservoirs for the encapsulation of guest cargos.[26−29] Mesopores have been used for the loading of photosensitizers for PDT against tumors.[30,31] On this ground, it is highly expected that well-defined mesoporous structures can also be employed to facilitate the encapsulation and delivery of sonosensitizers for efficient SDT. The specific advantages of mesopores for sonosensitizer delivery are their effectiveness for protecting sonosensitizers from physiological environment, enhanced tumor-accumulation, and sustained sonosensitizer release. In this work, we chose mesoporous organosilica nanoparticles (MONs) with molecularly organic−inorganic hybrid frameworks as sonosensitizer nanocarriers, rather than traditional MSNs with a pure Si−O−Si framework, on the basis that the elaborately designed MONs with biologically active organic groups in the framework (disulfide bond in this work) demonstrate intrinsic tumor microenvironment (TME)-responsive biodegradability and greatly improved biocompatibility/biosafety.[32−37]

In detail, biocompatible hollow MONs (designated as HMONs), successfully fabricated via a "chemical homology" strategy,[38] have been developed herein, for the first time, as the nanocarriers for the covalent anchoring of sonosensitizers (protoporphyrin, PpIX) onto the large surface area of the mesopores (designated as HMONs-PpIX). Paramagnetic manganese ions have been chelated into the porphyrin ring based on the metalloporphyrin chemistry (designated as HMONs-MnPpIX), which could act as the contrast agents for T_1-weighted magnetic resonance imaging (MRI). Their biodegradability, in vivo histocompatibility, and biocompatibility have been comprehensively evaluated to guarantee further clinical translation. Furthermore, the in vitro and in vivo therapeutic results have demonstrated the high SDT efficiency of HMONs-MnPpIX as multifunctional sonosensitizers for MRI-guided tumor-growth suppression.

2. EXPERIMENTAL SECTION

2.1. Materials and Reagents. Tetraethylorthosilicate (TEOS), ammonia solution (25−28%), and triethanolamine (TEA) were bought from Sinopharm Chemical Reagent Co. Bis(3-triethoxysilylproyl)disulfide (BTDS) was obtained from Lark Chemical Technology Co., Ltd. Cetanecyltrimethylammonium chloride (CTAC), (3-aminopropyl)triethoxysilane (APTES), MES, N-(3-(dimethylamino)propyl)-N′-ethylcarbodiimide hydrochloride (EDC), N-hydroxysuccinimide (NHS), protoporphyrin (PpIX), N,N-dimethylformamide (DMF), $MnCl_2 \cdot H_2O$, 1,3-diphenylisobenzofuran (DPBF), and glutathione (GSH) were obtained from Sigma-Aldrich. Methoxy PEG silane (M-SLN-2000) was purchased from Jenkem Technology Co., Ltd. Cell Counting Kit-8 (CCK-8) and phosphate buffer solution (PBS) were obtained from Shanghai Ruicheng Bio-Tech Co., Ltd. DAPI staining solution and DCFH-DA were bought from Beyotime Biotechnology. 2,2,6,6-Tetramethylpiperidine (TEMP), 3,8-diamino-5-[3-(diethylmethylammonio)propyl]-6-phenylphenanthridinium diiodide (PI), 3′,6′-di(O-acetyl)-4′,5′-bis[N,N-bis(carboxymethyl)aminomethyl]fluorescein, and tetraacetoxymethyl ester (Calcein-AM) were purchased from Dojindo Molecular Technologies, Inc. Deionized water was used in all experiments. All chemicals were used without further treatment.

2.2. Synthesis of Molecularly Organic−Inorganic Hybridized HMONs by a "Chemical Homology" Approach. Typically, CTAC aqueous solution (20 g, 10 wt%) and TEA aqueous solution (0.8 g, 10 wt%) were premixed and stirred in a water bath at 95 °C, followed by the addition of TEOS (1 mL) dropwise. The MSNs core was generated after a 1 h hydrolysis/condensation reaction. Mixed silicon sources, TEOS (1 mL) and BTDS (0.6 mL), were then added into the reaction system, which was left for reaction for another 4 h to form the MSNs@MONs core/shell structure. The white product was collected by centrifugation and washed with ethanol three times. The CTAC, as the structure-directing agent, was removed in a mixture of ethanol and concentrated HCl (37%) ($V_{ethanol}:V_{HCl}$ = 10:1) by extracting for 12 h at 78 °C three times; it was then dispersed into ethanol (20 mL) after washing with ethanol three times. Finally, MSNs@MONs solution (5 mL) was taken out to be redispersed into water (100 mL), followed by the addition of ammonia solution (2 mL). The etching process lasted for 3 h at 95 °C. Hollow-structured MONs (HMONs) were finally collected by centrifugation and washing with water.

2.3. Preparation of MES Solution. MES (0.025 mol) was dissolved into deionized water (200 mL), and then NaOH (1 mol/L) was added dropwise until the pH of the solution reached 5.5. The pre-prepared solution was carefully diluted to 250 mL in a volumetric flask to obtain MES solution (0.1 mol/L, pH = 5.5). The MES solution was stored at 2−4 °C for further use.

2.4. Anchoring Metalloporphyrin into the Mesopores of HMONs. The PpIX was introduced and anchored by an amidation reaction between the amino group and the carboxyl group. The metallic manganese element was then chelated into PpIX. Typically, the collected HMONs were dispersed in ethanol (100 mL), followed by the addition of APTES (1 mL) and then refluxing for 12 h at 80 °C to obtain the amino group-modified HMONs (HMONs-NH_2). HMONs-NH_2 were dispersed into MES solution (120 mL, 0.1 mol/L, pH = 5.5). EDC (35.2 mg) and NHS (6.8 mg) were then added. PpIX (10 mg) was slowly added and stirred at room temperature for 12 h. The mixture was centrifuged and washed with ethanol until the supernatant was clear to get HMONs-PpIX. Finally, $MnCl_2 \cdot H_2O$ (42 mg) was added into HMONs-PpIX-dispersed DMF (30 mL). The solution was refluxed at 140 °C for 1 h under an argon atmosphere for protection. The final product of HMONs-MnPpIX was obtained after centrifugation and washing with ethanol.

2.5. Surface PEGylation of HMONs-MnPpIX. Typically, HMONs-MnPpIX was dispersed into ethanol (100 mL) containing dissolved Methoxy PEG silane (25 mg), which was then refluxed at 80 °C for 12 h. The PEG molecules were covalently modified onto the surface of HMONs-MnPpIX by this conjugation process.

2.6. Characterization. Transmission electron microscopy (TEM) was conducted on a JEM-2100F electron microscope operated at 200 kV, which was used to observe the microstructure of HMONs. The morphology of HMONs was characterized by scanning electron microscopy (SEM) on a field emission Magellan 400 microscope (FEI Company). The specific surface area and pore size were detected by a N_2 adsorption−desorption isotherm on a Micrometitics Tristar 3000 system. UV−vis spectra were conducted on a UV-3101PC Shimadzu spectroscope. Zeta potential was tested on a Zetasizer Nanoseries instrument (Nano ZS90). Inductively coupled plasma atomic emission spectrometry (ICP-AES) was conducted on a VISTA instrument (Varian Company, American). The CLSM images were obtained using an FV 1000 camera, Olympus, Japan. All the US experiments were conducted using an ultrasound transducer (Chattanooga Co., U.S.A.). ESR characterization was performed on a Bruker EMX electron paramagnetic resonance (EPR) spectrometer.

2.7. Detecting $^1O_2$ by ESR. The generation of $^1O_2$ by HMONs-MnPpIX-PEG was detected by TEMP. Typically, HMONs-MnPpIX (500 μg/mL) was exposed to US irradiation (1.0 MHz, 1.5 W/cm^2, 50% duty cycle) for 120 s in the presence of TEMP (97 μM). The $^1O_2$ signal was immediately detected by the ESR spectrometer. As controls, the HMONs-MnPpIX + TEMP group, US + TEMP group, and US + HMONs-MnPpIX + TEMP group were also tested for comparison.

2.8. Biodegradation Evaluation of HMONs-MnPpIX-PEG in SBF Solution. In order to determine the structural evolution of HMONs-MnPpIX-PEG during the biodegradation process, they were incubated in simulated body fluid (SBF) at 37 °C under slow stirring. The partially biodegraded HMONs-MnPpIX-PEG was collected by centrifugation and directly observed by TEM characterization. Also,

the corresponding hydrodynamic particle-size distribution of HMONs-MnPpIX-PEG was detected by dynamic light scattering (DLS).

2.9. Cell Culture and Animals. *Cell Culture.* Breast cancer line 4T1 cells were used in all experiments, which were cultured in DMEM media. All the media were supplemented with 10% fetal bovine serum (FBS, Ruicheng Bio-Tech Co., Ltd., Shanghai), 100 units/mL penicillin, and 100 μg/mL streptomycin. The cells were cultured at 37 °C in a 5% CO_2 air atmosphere.

Animals. Healthy female Kunming mice (~20 g) and 4-week-old female BALB/c nude mice (~15 g) were obtained from Shanghai Experimental Animal Center (Shanghai). All animal experiments were conducted under the guideline approved by the Institutional Animal Care and Use Committee of the Shanghai Institute of Materia Medica, Chinese Academy of Sciences.

2.10. MR Imaging of Tumor by HMONs-MnPpIX-PEG. HMONs-MnPpIX-PEG was intravenously injected into 4T1 tumor-bearing mice at the Mn dose of 0.07 mg/kg when the tumor volume reached around 200 mm³ after 4T1 cancer-cell implantation. The T_1-weighted MR imaging of mice were acquired after the different intervals followed by HMONs-MnPpIX-PEG administration.

2.11. Biodegradation Assay of HMONs-MnPpIX-PEG at Cell Level. The intracellular biodegradation behavior of HMONs-MnPpIX-PEG and its structural evolution were directly observed by bio-TEM observation. Typically, HMONs-MnPpIX-PEG (100 μg/mL in DMEM) was co-incubated with 4T1 cancer cells. After different co-incubation durations (1, 3, 5, and 7 d), the cells were harvested, fixed, and sectioned for bio-TEM characterization.

To quantify the biodegradation, 4T1 cells (n = 3) co-incubated with HMONs-MnPpIX-PEG (100 μg/mL in DMEM) for 1, 3, 5, and 7 d were washed with PBS three times and then collected and melted by chloroazotic acid (V_{HCl}:V_{HNO3} = 3:1). The residual Mn and Si contents in 4T1 cells were determined by ICP-OES test.

2.12. Intracellular Endocytosis by CLSM Observation. Typically, 4T1 cells at a density of 1×10^5 were seeded into the CLSM-specific dish (35 mm × 10 mm, Corning Inc., New York) and incubated for 12 h until they were adhered to the wall of the dish. Then, the culture media was replaced with HMONs-MnPpIX-PEG (1 mL, 20 μg/mL in DMEM), which was then cultured for 4 and 8 h. DAPI (100 μL) was added into the dish to stain the cell nuclei. The cells were then observed by CLSM after staining for 15 min.

2.13. In Vitro $^1O_2$ Generation. The cells were co-incubated with HMONs-MnPpIX-PEG (1 mL, 100 μg/mL in DMEM) at 37 °C for 3 h. Then, the cells were treated by US irradiation (1.0 MHz, 1.5 W/cm², 50% duty cycle, 1 min) and incubated for another 4 h. The culture media was replaced with DCFH-DA (100 μL, 1 μL/9 μL in DMEM) for another 15 min staining. The cells were finally washed with PBS three times and observed by CLSM.

2.14. CLSM Observation of the Sonotoxicity of HMONs-MnPpIX-PEG. The cell-treatment protocol is almost the same as the above-mentioned CLSM observation on $^1O_2$ generation except the substitution of DCFH-DA with Calcein-AM (100 μL, 20 μM) and PI (100 μL, 20 μM), to stain the living and dead cells, respectively.

2.15. In Vitro SDT Efficiency of HMONs-MnPpIX-PEG against Cancer Cells. 4T1 cells were maintained in DMEM containing 10% fetal bovine serum and seeded in 96-well plates at a density of 1×10^4 cells per well for 12 h to ensure that they were adherent to the plate. Then, HMONs-MnPpIX-PEG at different concentrations were added into the well and co-incubated for another 24 h. The culture media was replaced with CCK-8 (100 μL, V_{CCK-8}:V_{DMEM} = 1:9) and the cell viabilities were measured on a microplate reader at the wavelength 450 nm after 90 min. To investigate the sonotoxicity of HMONs-MnPpIX-PEG, four groups including HMONs-MnPpIX-PEG + US group, HMONs-MnPpIX-PEG group, US-only group and control group without treatment were evaluated simultaneously. The cell viabilities were tested similar to the above-mentioned protocol after US (1.0 MHz, 1.5 W/cm², 50% duty cycle, 1 min) irradiation and further incubation for 3 h.

2.16. In Vivo Biocompatibility Assay. Healthy female Kunming mice (n = 6 in each group) were adopted for evaluation. Different doses of HMONs-MnPpIX-PEG (5, 10, and 20 mg/kg) were

intravenously injected into the mice. The mice without any treatment were used as the control group. The body weight of mice was recorded every 2 days. After 1 month of feeding, the mice were sacrificed and their blood samples and organs (heart, liver, spleen, lung, and kidney) were taken out for the assessment, including various blood indexes and hematoxylin and eosin (H&E) staining.

2.17. In Vivo Evaluation of SDT Efficiency against Tumor Growth. Typically, female BALB/c nude mice were subcutaneously injected with 4T1 cells to establish the tumor xenograft. When the tumor volume reached 40 mm³, the mice were divided into four groups including control group, HMONs-MnPpIX-PEG + US group, HMONs-MnPpIX-PEG group and US group (n = 5 in each group). The mice in HMONs-MnPpIX-PEG + US group and HMONs-MnPpIX-PEG group were intravenously injected with HMONs-MnPpIX-PEG (10 mg/kg). Only the mice HMONs-MnPpIX-PEG + US group and US group were treated by US irradiation (1.0 MHz, 2.3 W/cm², 50% duty cycle, 5 min) after injection of HMONs-MnPpIX-PEG for 3 h and 5 d. The tumor volume ($V = (ab^2)/2$, where a and b refer to the largest length and width of tumor, respectively) was recorded and photographed every 2 days. The relative tumor volume was calculated by the formula of $(W/W_0) \times 100\%$ (where W_0 is the tumor weight of the control group, and W represents the tumor weight of the experimental groups). The tumor-inhibition percentage of each group was analyzed by the expression of $(1 - V/V_0) \times 100\%$ (where V_0 is the tumor volume of the control group and V the volume of the other groups). At the end of treatment, the tumor was dissected and stained by H&E, TdT-mediated dUTP Nick-End Labeling (TUNEL), and Ki-67 for histological analysis.

3. RESULTS AND DISCUSSION

Hollow mesoporous organosilica nanoparticles (HMONs) of molecularly organic−inorganic hybridized framework were initially synthesized as the matrix for the following anchoring of Mn-protoporphyrin (MnPpIX). HMONs were chosen based on their unique nanostructure and composition. Disulfide bond (S−S) was covalently hybridized into the framework of HMONs to guarantee the improved biodegradation responsive to the mildly reducing microenvironment of tumor tissue.[34,39] The hollow nanostructure of HMONs could be further used for enhancing the loading capacity for guest molecules.[40,41] Typically, HMONs were synthesized by using SiO_2 as the hard template based on our previously developed "structural difference-based selective etching" strategy (Figure 1a).[40] Bis(3-triethoxysilylpropyl)disulfide (BTDS) was adopted to form the organosilica shell with disulfide bond-incorporated framework. The as-synthesized HMONs were initially grafted with amino group via the typical (3-Aminopropyl)triethoxysilane (APTES) modification (HMONs-NH$_2$). Protoporphyrin (PpIX) was then covalently linked onto the mesopore surface of HMONs-NH$_2$ via the dehydration reaction between amino groups of HMONs-NH$_2$ and carboxyl groups of PpIX (HMONs-PpIX). Manganese ions could be easily chelated into the porphyrin rings of (HMONs-MnPpIX) based on a chelating reaction. To further improve the stability of HMONs-MnPpIX in physiological condition (Figure 1b), the surface of composite sonosensitizer was further PEGylated by methoxy PEG silane (designated as HMONs-MnPpIX-PEG).

The mesoporous structure of HMONs is unique, facilitating the anchoring of sonosensitizers for imaging-guided SDT. On one hand, the large surface area of HMONs provides abundant anchoring sites for covalently grafting small organic sonosensitizers into the mesopores with high loading amounts (Figure 1c). When the nanosized sonosensitizers are irradiated by US, the SDT-generated ROS can freely diffuse out of the mesopores to exert the therapeutic function. On the other hand, the paramagnetic Mn centers in MnPpIX are highly
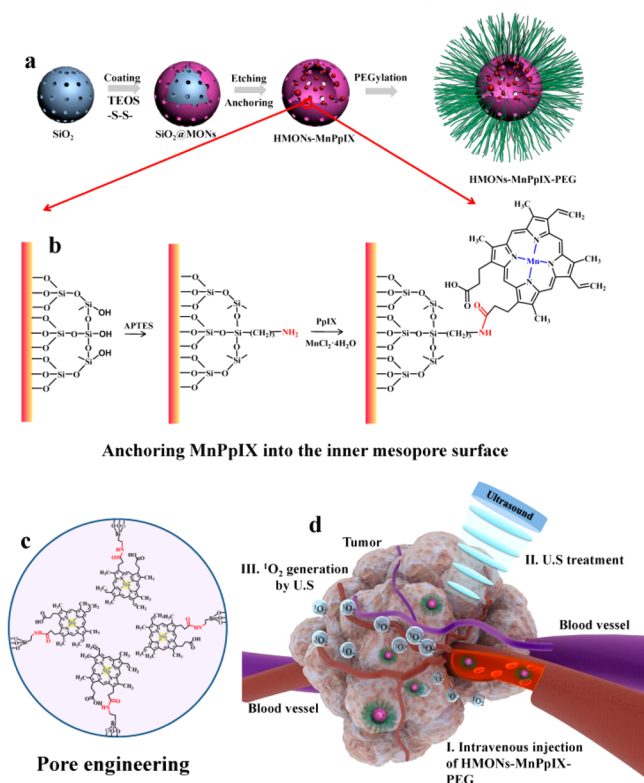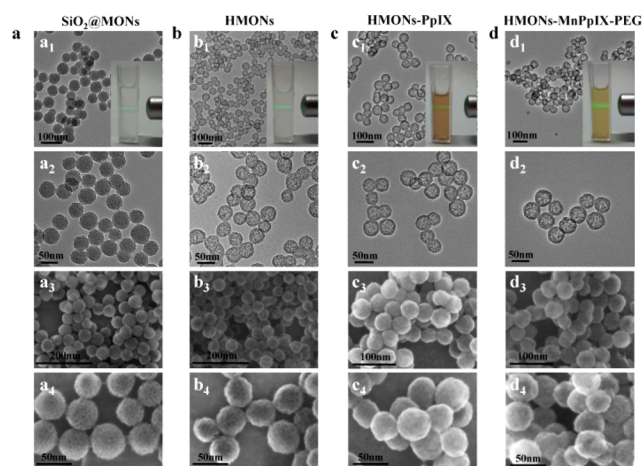
Figure 1. Schematic illustration of (a) the synthesis of HMONs-MnPpIX-PEG, (b) detailed synthetic steps of grafting MnPpIX into the inner mesopore surface of HMONs to fabricate HMONs-MnPpIX-PEG based on metalloporphyrin chemistry, (c) The scheme of MnPpIX covalently grafted into the mesopores, (d) blood transport/tumor accumulation of HMONs-MnPpIX-PEG and its SDT effect on cancer treatment.

Figure 2. TEM images of (a_1 and a_2) SiO$_2$@MONs, (b_1 and b_2) HMONs, (c_1 and c_2) HMONs-PpIX. and (d_1 and d_2) HMONs-MnPpIX-PEG at different magnifications, and SEM images of (a_3 and a_4) SiO$_2$@MONs, (b_3 and b_4) HMONs, (c_3 and c_4) HMONs-PpIX. and (d_3 and d_4) HMONs-MnPpIX-PEG at different magnifications. Insets of a_1, b_1, c_1, and d_1 are the corresponding photographic images of sample solutions showing the typical Tyndall effect.

c_1, and d_1), indicating the successful grafting of PpIX within the mesopores.

The successful anchoring of PpIX and MnPpIX was further demonstrated by UV−vis characterization. Porphyrins and their metal derivatives typically show their characteristic spectra, which can also be found in HMONs-PpIX and HMONs-MnPpIX (Figure 3a). The specific absorption of porphyrins is

dispersed within the mesopores, which facilitates the direct interaction with hydrogen protons of water molecules,[42−45] and consequently produces significantly improved T_1-weighted MRI performance. Therefore, the synthesized HMONs-MnPpIX-PEG can freely transport within the blood vessel and accumulate into the tumor tissue via typical enhanced permeability and retention (EPR) effect. When they are irradiated by external US, they can generate the toxic ROS for inducing the apoptosis/death of cancer cells. The MR imaging function of HMONs-MnPpIX-PEG provides the guidance for SDT and the following therapeutic outcome monitoring (Figure 1d).
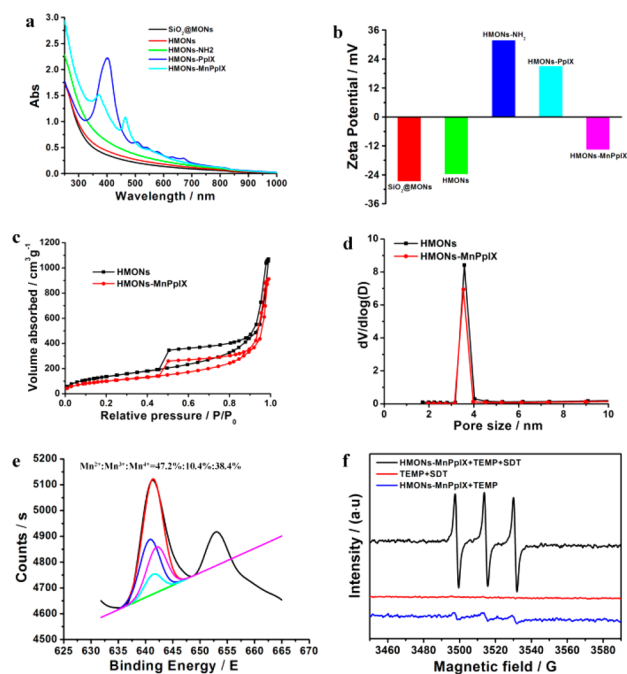
The initially synthesized solid silica nanoparticles could be easily coated by a MONs layer because the hydrolysis and condensation processes of BTDS as the bissilylated organosilica source (for MONs layer) are similar in nature to that of tetraethylorthosilicate (TEOS) in the formation of silica core. Uniform core/shell structured SiO$_2$@MONs were synthesized with high dispersity and well-defined mesopores in the shell (Figure 2a and 2a_1-a_4). The silica core was completely removed after treating SiO$_2$@MONs in ammonia solution to form HMONs (Figure 2b and 2b_1-b_4). HMONs still maintain the high dispersity and uniform spherical morphology after the etching process. The following PpIX grafting and subsequent Mn chelating did not change the morphology and nanostructure of HMONs (Figure 2c,d), but the color of nanoparticles changed from the white to mild black (insets in Figure 2a_1, b_1,

Figure 3. (a) UV−vis spectra and (b) Zeta potential of SiO$_2$@MONs, HMONs, HMONs-NH$_2$, HMONs-PpIX, and HMONs-MnPpIX. (c) N$_2$ adsorption−desorption isotherms and (d) the corresponding pore-size distributions of HMONs and HMONs-MnPpIX. (e) XPS spectrum of HMONs-MnPpIX. (f) ESR spectra of HMONs-MnPpIX with and without US treatment. TEMP without US irradiation was used as a control for comparison.

attributed to the π electrons belonging to porphyrin rings, which means that the variations of the π electrons may cause changes in their spectra.[46] Free porphyrin molecules have four characteristic absorption peaks at 500−800 nm and a strong absorption peak at about 420 nm. The difference from free porphyrin lies in the number reduction of the original four characteristic absorption peaks at 500−800 nm to two peaks after chelating metal Mn ions to porphyrins rings.[47] For HMONs-PpIX, there exist five peaks in 350−700 nm and a strong absorption peaks at 400 nm. The shifts of peak positions of porphyrin might be attributed to the structure changes of π electrons when the porphyrin molecules are confined onto the surface of mesopores. The number of absorption peaks of HMONs-MnPpIX decreases to two in 350−700 nm, similar to the changes from porphyrin to metal porphyrin, indicating the successful chelating of Mn ions into the porphyrin rings within the mesopores.

The series changes on Zeta potential of each grafting step further indicate the successful grafting of MnPpIX on the surface of mesopores (Figure 3b). The MnPpIX modification of HMONs could still maintain the well-defined mesoporous structure as demonstrated by N_2 absorption−desorption isotherms of HMONs and HMONs-MnPpIX (Figure 3c). The BET surface areas of HMONs and HMONs-MnPpIX are 515 m^2/g and 381 m^2/g, and their corresponding pore volumes are 1.18 and 0.94 cm^3/g, respectively. The slight decreases of surface area and pore volume of HMONs after MnPpIX anchoring further demonstrates the incorporation of MnPpIX into the mesopores. The initial mesopore size of HMONs was 3.6 nm, which then decreased to about 3.4 nm after MnPpIX modification (Figure 3d). XPS spectrum of HMONs-MnPpIX clearly shows the Mn signals, and the relative contents of bivalent, trivalent and quadrivalent Mn were determined to be 47.2%, 10.4% and 38.4%, respectively (Figures 3e and S1). To show the SDT capability of HMONs-MnPpIX and the corresponding mechanism of SDT procedure, electron spin resonance (ESR) spectrum of HMONs-MnPpIX was acquired after the exposure to US exposure. 2,2,6,6-Tetramethylpiperidine (TEMP) was used to scavenge $^1O_2$, which yielded the nitroxide radical TEMPOL, a paramagnetic product possessing unpaired electrons on the NO groups. Interaction between the unpaired electronic spin and the nitrogen ^{14}N nucleus may cause the ESR signal to split into three narrow lines.[48] In ESR spectra (Figure 3f), characteristic $^1O_2$-induced signals can be observed in the HMONs-MnPpIX + US group. Because PpIX is also a photosensitizer, there exist weak signals in HMONs-MnPpIX group under the exposure to light during the tests. To quantitatively analyze the generation of singlet oxygen, the typical 1,3-diphenylisobenzofuran (DPBF) agent was adopted. The generation of singlet oxygen can oxidize DPBF to decrease its absorbance intensity in UV−vis spectrum at the wavelength of 410 nm. It can be found that the absorbance intensity of DPBF decreases significantly upon the exposure of DPBF to US in the presence of sonosensitizer for 6 min (Figure S2), demonstrating the quick production of singlet oxygen during the sonodynamic process.

The biodegradation issue of the developed composite nanosystem as an efficient sonosensitizer is of great significance for clinical translation. One of the design priorities of our nanosystem is to choose easily biodegradable HMONs by molecularly hybridizing biologically active organic groups into the framework of mesoporous silica. Therefore, the biodegradation behavior of the nanosized sonosensitizer (HMONs-

MnPpIX-PEG) was systematically investigated. Because of the presence of reducing-responsive disulfide bond in the framework, the structural evolution of HMONs-MnPpIX-PEG during the biodegradation process was monitored in simulated body fluid (SBF) at different glutathione (GSH) concentrations (0, 5, and 10 mM, simulating the tumor reducing microenvironment) by TEM observation (Figure 4). The corre-
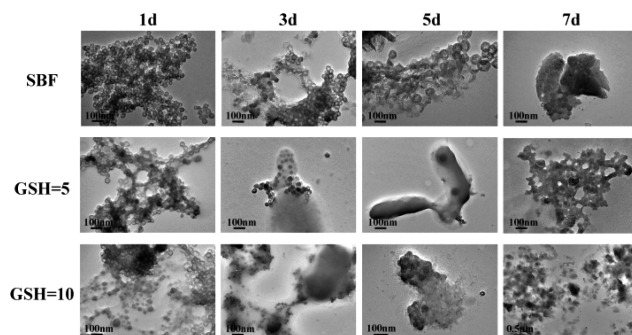

Figure 4. TEM images of HMONs-MnPpIX-PEG (0.1 mg/mL) in SBF at different GSH concentrations (0, 5, and 10 mM) for varied incubation durations (1, 3, 5, and 7 d), showing the structural evolution of HMONs-MnPpIX-PEG during the biodegradation process.

sponding particle-size distribution was also recorded (Figure S3). It has been found that HMONs-PpIX-PEG exhibits much faster biodegradation in SBF under reducing condition compared to the biodegradation in SBF without GSH. HMONs-PpIX-PEG still keeps the intact spherical morphology in 1 d biodegradation in pure SBF, but it has suffered the significant biodegradation in the same period in SBF at the GSH concentration of 5 mM. The higher GSH concentration (10 mM) in SBF causes more significant biodegradation. This unique reducing-responsive biodegradation facilitates the SDT against tumor because of the mildly reducing microenvironment of tumor. The fast biodegradation of HMONs-MnPpIX-PEG will enable the quick releasing of the loaded MnPpIX for subsequently enhanced SDT efficiency. Importantly, HMONs-MnPpIX-PEG also shows a moderate biodegradation behavior in pure SBF in several days of incubation. This means that these nanosized sonosensitizers could biodegrade in vivo and excrete out of the body if they could enter the normal organs/tissues, showing relatively high biosafety for further potential clinical translation.

The biodegradation behavior and structural evolution of HMONs-MnPpIX-PEG were further evaluated in cells. After co-incubation of HMONs-PpIX-PEG with 4T1 cells for different durations (1, 3, 5, and 7 d), the cells were harvested, fixed and cut into ultrathin sections for bio-TEM observation. It has been found that HMONs-MnPpIX-PEG could be efficiently endocytosized into cancer cells (Figure 5a). Importantly, the significant intracellular biodegradation has been found. The morphology and hollow nanostructure of HMONs-MnPpIX-PEG can be distinguished within a short time period (1 d, Figure 5a), and then partial nanoparticles have experienced significant biodegradation (3 d, Figure 5b). The extended incubation causes a large extent intracellular biodegradation (5 d, Figure 5c). The 7 d intracellular co-incubation induces almost the complete degradation of HMONs-MnPpIX-PEG as it is difficult to find the unbiodegraded nanoparticles intracellularly by bio-TEM observa-
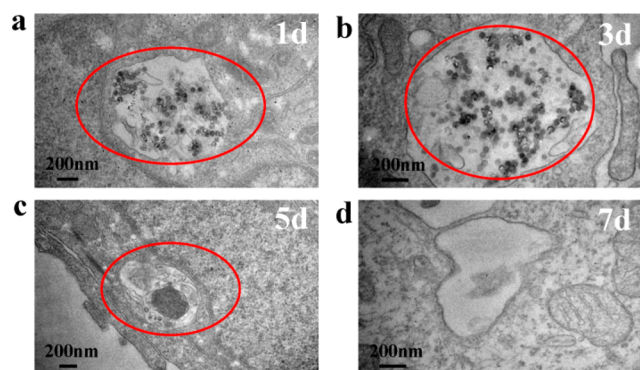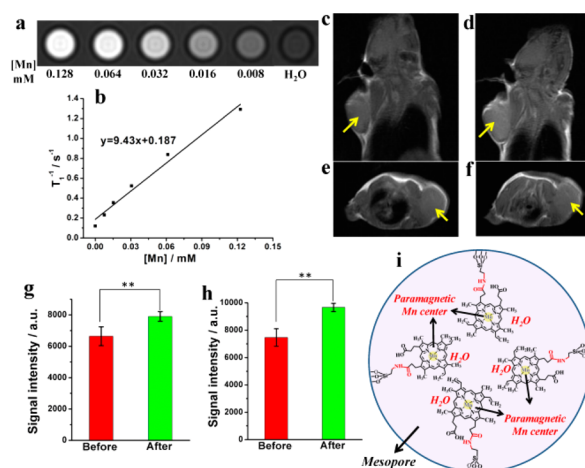
Figure 5. Intracellular biodegradation and structural evolution of HMONs-MnPpIX-PEG in 4T1 cancer cells by bio-TEM observation after the intracellular biodegradation for different durations (1, 3, 5, and 7 d).

Figure 6. (a) *In vitro* T_1-weighted MR imaging of HMONs-MnPpIX-PEG aqueous solutions at varied Mn concentrations, and (b) corresponding $\Delta 1/T_1$ versus Mn concentration of HMONs-MnPpIX-PEG buffer solutions. *In vivo* T_1-weighted MR imaging of 4T1 tumor-bearing mice (c, axial and e, coronal) before and (d, axial and f, coronal) after intravenous administration of HMONs-MnPpIX-PEG, and (g, axial and h, coronal) corresponding T_1-weighted MRI signal intensity of tumor before and after the injection of HMONs-MnPpIX-PEG (**$p < 0.01$). (i) Schematic illustration of highly dispersed paramagnetic Mn centers within the mesopores, which facilitates their interaction with the protons of water molecules.

tion (Figure 5d). The quantitative analyses of intracellular Si and Mn content during the biodegradation process were also conducted (Figure S4). It has been found that both the intracellular Mn and Si contents decrease with the increase of co-incubation time, which further demonstrates the intracellular biodegradation of the nanosystem. The *in vitro* assay in either SBF or intracellular condition strongly demonstrates the easy biodegradation behavior, which could potentially guarantee the controlled biodegradation *in vivo*.

The potential diagnostic-imaging guidance is of practical significance for efficient SDT because the pre-positioning of target sites by imaging assistance will enable the direct and precise US focusing on the tumor tissue during the following US irradiation, which can mitigate the possible damages of US to the surrounding normal tissues and improve the therapeutic precision. To achieve this goal, metalloporphyrin chemistry was employed to anchor paramagnetic Mn centers into porphyrin rings. The multifunctional sonosensitizer HMONs-MnPpIX-PEG shows the marked *in vitro* T_1-weighted positive MRI contrast (Figure 6a) with a relaxivity r_1 of as high as 9.43 mM^{-1} s^{-2} (Figure 6b), which is almost 2-fold that of clinical Gd-based complex.[49,50] It is noted that the biodegradation of HMONs-MnPpIX-PEG could result in the improved T_1-MRI performance of MnPpIX (Figure S5) because the biodegradation of HMONs-MnPpIX and releasing of MnPpIX could give rise to the much enhanced accessibility of Mn paramagnetic centers to water molecules compared to un-degraded HMONs-MnPpIX-PEG with paramagnetic centers being within the mesopores, thus the positive T_1 performance would be significantly enhanced after the biodegradation.

Importantly, the intravenous administration of HMONs-MnPpIX-PEG into 4T1 tumor-bearing mice significantly elevates the *in vivo* T_1-weighted positive contrast of tumor (Figure 6c−f), which is further revealed by the increase of T_1-weighted MRI signal intensity after the injection of HMONs-MnPpIX-PEG (Figure 6g,h). The high T_1-weighted MRI performance of HMONs-MnPpIX-PEG is due to the thorough dispersity of paramagnetic Mn centers within the mesopores. The penetrating mesopores also facilitate the diffusion of water molecules, thus maximizing the accessibility of protons on water molecules to Mn centers in the mesopores (Figure 6i).[42,51] This result not only demonstrates the possibility of HMONs-MnPpIX-PEG as the contrast agents for MRI guidances of SDT, but also gives the first evidence that

nanoparticulate sonosensitizers can be endowed with diagnostic-imaging functionality for theranostic applications.

The *in vitro* SDT efficiency of HMONs-MnPpIX-PEG was evaluated in detail. First, confocal laser scanning microscopic (CLSM) images show that HMON-MnPpIX-PEG could efficiently enter the cancer cells as evidenced by the presence of strong intracellular red fluorescence originated from MnPpIX of HMONs-MnPpIX-PEG (4 h co-incubation, Figure 7a). The red fluorescence intensity was enhanced at extended incubation durations (8 h co-incubation, Figure 7b). To reveal the intracellular mechanism of HMONs-MnPpIX-PEG as sonosensitizers in killing the cancer cells, the intracellular ROS levels were determined by using 2′-7′-dichlorofluorescein diacetate (DCFH-DA), which could be converted from non-fluorescence status into fluorescent 2,7-dichlorofluorescein (DCF) by ROS (Figures 7c−f and S6). It can be found that HMONs-MnPpIX-PEG exhibits weak green fluorescence because of the photosensitive effect of MnPpIX (Figure 7d). Importantly, HMONs-MnPpIX-PEG combined with US irradiation (1.0 MHz, 1.5 W/cm^2, 50% duty cycle, 1 min) induces the mass production of intracellular ROS as demonstrated by the strong green fluorescence in cancer cells (Figures 7f and S6). Comparatively, neither control cells nor US irradiation only could induce the intracellular fluorescence (Figure 7c,f). Combined with ESR result (Figure 3f), it can be deduced that HMONs-MnPpIX-PEG as sonosensitizers can generate ROS such as singlet oxygen ($^1O_2$) under US irradiation to induce the toxic effect and achieve the therapeutic function afterward.

The sonotoxicity of HMONs-MnPpIX-PEG against cancer cells was initially characterized by CLSM observation. After co-incubation of HMONs-MnPpIX-PEG with 4T1 cells for 4 h, US (1.0 MHz, 1.5 W/cm^2, 50% duty cycle, 1 min) was adopted to irradiate the cells followed by Calcein AM and propidium iodide (PI) co-staining. The strong green fluorescence and
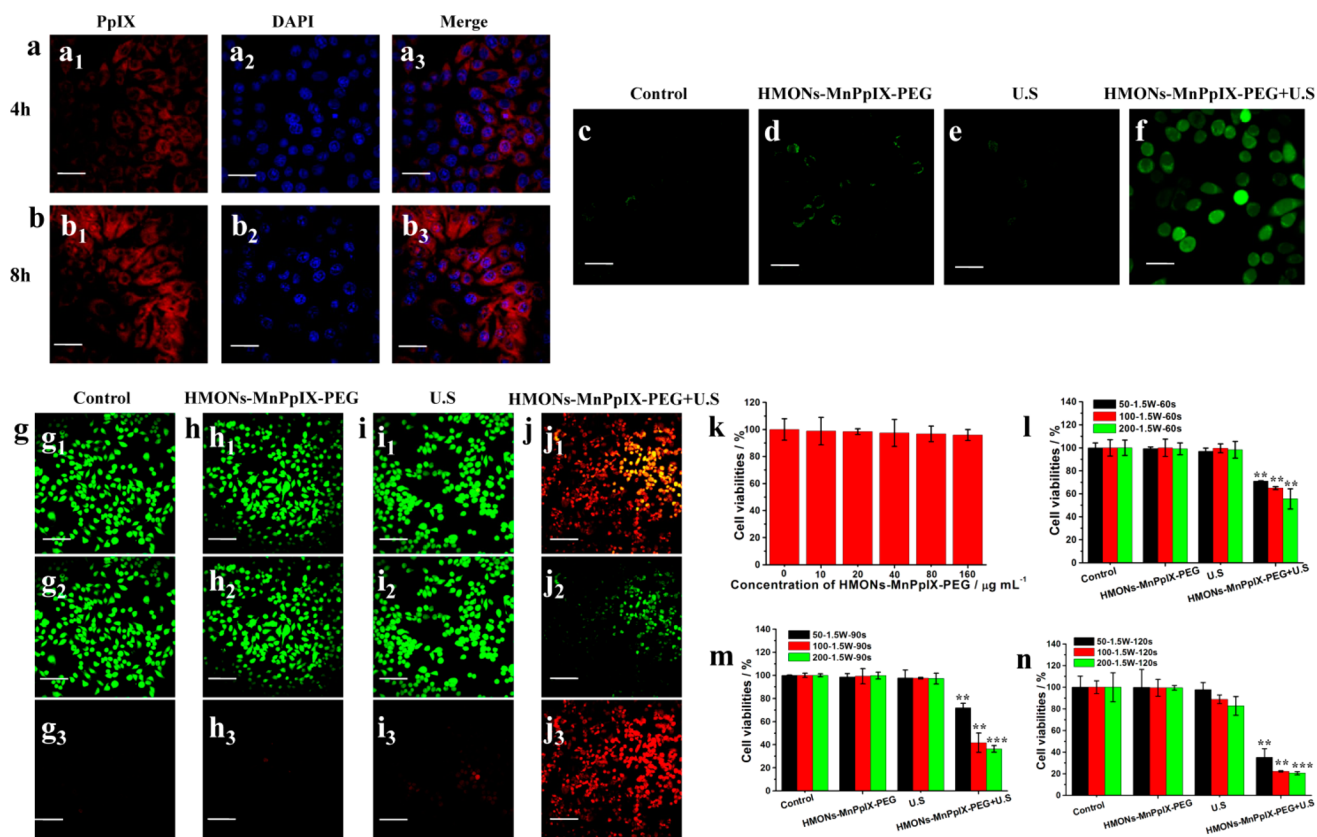
Figure 7. CLSM images of 4T1 cells after co-incubation with HMONs-MnPpIX-PEG for (a) 4 h and (b) 8 h. ([HMONs-MnPpIX-PEG] = 20 μg/mL; Red fluorescence: MnPpIX in HMONs-MnPpIX-PEG, blue fluorescence: DAPI). Scale bar = 20 μm. CLSM images of 4T1 cells stained with DCFH-DA after different treatments of (c) control (without any treatment), (d) HMONs-MnPpIX-PEG only, (e) US only and (f) HMONs-MnPpIX-PEG combined with US irradiation. Scale bar = 20 μm. CLSM images of 4T1 cells stained by calcein AM and PI after various treatments of (g) control (without any treatment), (h) HMONs-MnPpIX-PEG only, (i) US only, and (j) HMONs-MnPpIX-PEG combined with US irradiation (Green fluorescence: calcein AM representing living cells, red fluorescence: PI representing dead cells). Scale bar = 60 μm. (k) Cell viabilities of 4T1 cells after co-incubation with HMONs-MnPpIX-PEG for 24 h. (l−n) Cell viabilities of 4T1 cells after exposed to US irradiation for different time durations (l, 30 s; m, 90 s; n, 120 s) at varied HMONs-MnPpIX-PEG concentrations of 50, 100, and 200 μg/mL. The adopted US power density was 1.5 W/cm^2. (Corresponding to control group, **$p < 0.01$, ***$p < 0.001$.)

neglectable red fluorescence in control, US only and HMONs-MnPpIX-PEG groups indicates that the cells keep the intact physiological state (Figure 7g−i). Comparatively, the group of HMONs-MnPpIX-PEG combined with US irradiation exhibits strong red fluorescence originated from PI staining (Figure 7j and S7), demonstrating that the SDT process assisted by HMONs-MnPpIX-PEG has caused the substantial cell death. Especially, HMONs-MnPpIX-PEG itself exhibits negligible cytotoxicity by CCK-8 assay (Figure 7k). The SDT in combination with HMONs-MnPpIX-PEG induces markedly high therapeutic efficiency featuring greatly suppressed cell proliferation and massive cell death (Figure 7l−n), which are also HMONs-MnPpIX-PEG concentration- and US irradiation duration-dependent.

The *in vivo* biocompatibility of HMONs-PpIX-PEG was extensively evaluated to guarantee their safety for *in vivo* use. Healthy female Kunming mice were intravenously injected with HMONs-MnPpIX-PEG at varied doses of 5, 10, and 20 mg/kg. The group without receiving HMONs-MnPpIX-PEG was set as the control group. The body weights of the mice were recorded and their blood indexes were tested at the end of evaluations. No significant body-weight losses of mice were observed after receiving HMONs-MnPpIX-PEG at different doses during one-month feeding (Figure S8). The blood indexes in HMONs-MnPpIX-PEG group show no significant changes compared to those in the control group (Figure S9). The tissue sections of heart, liver, spleen, lung, and kidney stained by H&E reveal no apparent pathological changes (Figure S10). These preliminary data indicate the high biocompatibility of as-synthesized HMONs-MnPpIX-PEG for *in vivo* SDT.

The easy biodegradation, high biocompatibility, and intriguing *in vitro* SDT efficiency encourage the further *in vivo* evaluation of SDT efficiency against cancer, which was assessed on 4T1 tumor xenograft in nude mice. HMONs-PpIX-PEG could easily transport within the blood vessel with a blood half-life of 0.914 h (Figure S11), efficient tumor accumulation and facile excretion out of the body (Figure S12). The tumor-bearing mice were randomly divided into four groups: control, HMONs-MnPpIX-PEG, US only and HMONs-MnPpIX-PEG + US groups. After the intravenous administration of HMONs-MnPpIX-PEG for 3 h, US (1.0 MHz, 2.3 W/cm^2, 50% duty cycle, 5 min) was directly irradiated on the tumor. The US irradiation was repeated on the fifth day (Figure 8a). It has been found that the tumor growth could be significantly suppressed in the HMONs-MnPpIX-PEG + US group compared to the other three groups (Figure 8b,c). The tumor-inhibition rate of HMONs-MnPpIX-PEG + US group reaches 75.4%, substantially higher than those of HMONs-MnPpIX-PEG group (17.4%) and US only group (43.1%). Photographic images of tumor at the end of treatments also
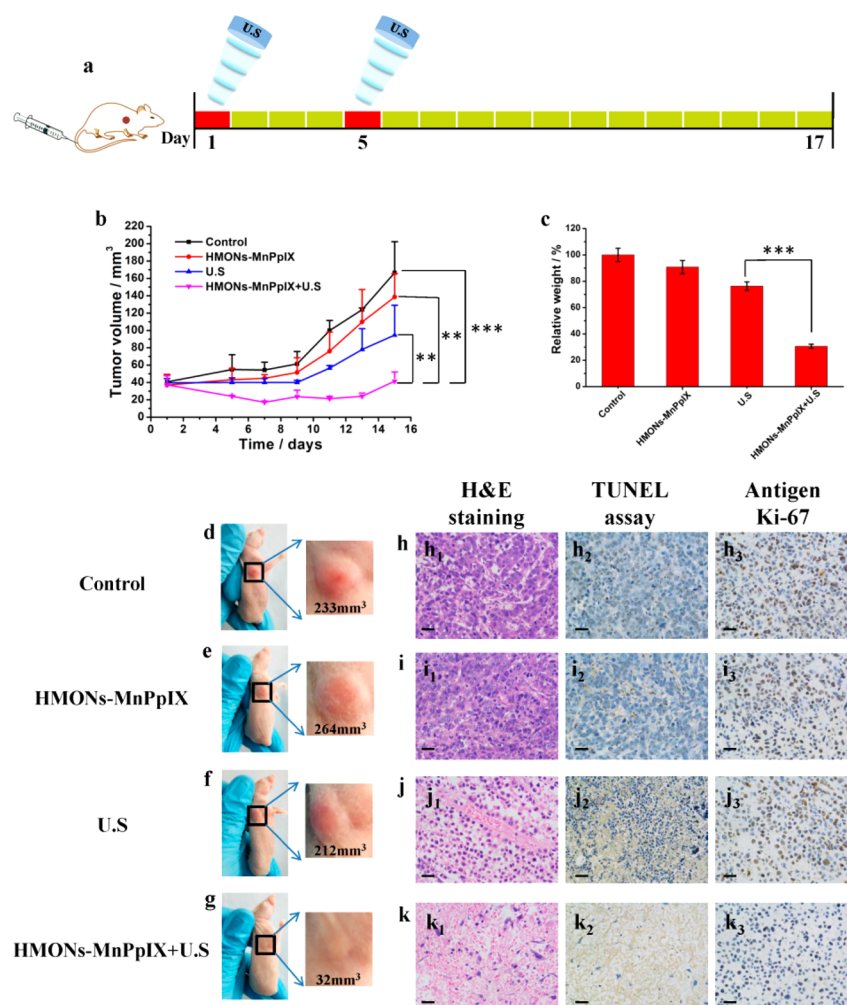
Figure 8. (a) *In vivo* therapeutic protocol of SDT on mice tumor xenograft. (b) Tumor-volume change as a function of feeding time after different treatments of control group, HMONs-MnPpIX-PEG group, US only group and HMONs-MnPpIX-PEG + US group, and (c) corresponding tumor weights acquired at the end of treatments ($**p < 0.01$, $***p < 0.001$). (d−g) Photographic images of tumor at the end of the treatments. Optical microscopic images of tumor sections stained by hematoxylin and eosin (H&E), TdT-mediated dUTP Nick-End Labeling (TUNEL) and Ki-67 from the groups of (h) control, (i) HMONs-MnPpIX-PEG, (j) US, and (k) HMONs-MnPpIX-PEG + US.

show the smallest tumor size in the HMONs-MnPpIX-PEG + US group compared to the other three groups (Figures 8d−g and S13).

The mechanism of high SDT efficiency by using HMONs-MnPpIX-PEG + US as the sonosensitizers were further revealed by pathological sections stained by H&E, TUNEL, and Ki-67 (Figure 8h−k). As shown in the H&E-stained tumor section (Figure $8h_1$, i_1, j_1, and k_1), there is only a small portion of purple blue (nuclei stained by hematoxylin) area in the HMONs-MnPpIX-PEG + US group, indicating that the majority of cancer cells have suffered apoptosis and necrosis. From the TUNEL assay result (Figure $8h_2$, i_2, j_2, and k_2), the number of apoptotic cells stained dark-brown in the HMONs-MnPpIX-PEG + US group is much less than those of the other control groups. The cell proliferation was assessed by Antigen Ki-67 (Figure $8h_3$, i_3, j_3, and k_3) as Ki-67 can stain the proliferative cells into brown. It can be found that the HMONs-MnPpIX-PEG + US group keeps the least brown cells and performs excellent inhibiting effect on cell proliferation.

4. CONCLUSIONS

In summary, we have successfully developed, for the first time, a nanoformulated sonosensitizer for highly efficient MRI-guided SDT against cancer, which aims to overcome the critical drawbacks of traditional PDT and develop more efficient therapeutic modality for cancer treatment. This approach takes the advantages of biodegradable mesoporous organosilica-based nanosystems for the fabrication of sonosensitizers with high theranostic performance. The well-defined mesoporous structure facilitates the high loading of sonosensitizers (PpIX in this work) and the subsequent chelating of paramagnetic transitional metal Mn ions based on metalloporphyrin chemistry. The penetrating mesostructure of large surface area also maximize the accessibility of protons on water molecules to the encapsulated paramagnetic Mn ions, endowing the composite sonosensitizers with excellent MR imaging performance for SDT guidance and monitoring. Importantly, the developed multifunctional sonosensitizers (HMONs-MnPpIX-PEG) are easily biodegradable and highly biocompatible. Intriguingly, the high SDT efficiency has been comprehensively demonstrated both *in vitro* for inducing the cancer-cell death and *in vivo* for suppressing the tumor growth. The mechanism

of high SDT efficiency assisted by HMONs-MnPpIX-PEG has also been revealed. It is highly expected that the developed nanotechnology-enhanced SDT strategy based on elaborately designed high-performance multifunctional sonosensitizers will pave a new way for efficient cancer treatments by taking advantage of biomedical US therapy (noninvasiveness, convenience, cost-effectiveness, etc.) and nanomedicine.

■ ASSOCIATED CONTENT

Ⓢ Supporting Information

The Supporting Information is available free of charge on the ACS Publications website at DOI: 10.1021/jacs.6b11846.

> Additional characterization data for HMONs-MnPpIX and intracellular uptake and *in vivo* biocompatibility of HMONs-MnPpIX-PEG, including Figures S1−S13 (PDF)

■ AUTHOR INFORMATION

Corresponding Authors

*chenyu@mail.sic.ac.cn
*yfzhu@usst.edu.cn
*jlshi@mail.sic.ac.cn

ORCID Ⓘ

Yu Chen: 0000-0002-8206-3325
Jianlin Shi: 0000-0001-8790-195X

Author Contributions

‖P.H. and X.Q. contributed equally to this manuscript.

Notes

The authors declare no competing financial interest.

■ ACKNOWLEDGMENTS

■ REFERENCES

(1) Siegel, R.; Naishadham, D.; Jemal, A. *CA-Cancer J. Clin.* **2013**, *63*, 11−30.

(2) Schmidt, C. *Nature* **2015**, *527*, S10−S11.

(3) LaVan, D. A.; McGuire, T.; Langer, R. *Nat. Biotechnol.* **2003**, *21*, 1184−1191.

(4) Smyth, M. J.; Godfrey, D. I.; Trapani, J. A. *Nat. Immunol.* **2001**, *2*, 293−299.

(5) Chaffer, C. L.; Weinberg, R. A. *Science* **2011**, *331*, 1559−1564.

(6) Dolmans, D.; Fukumura, D.; Jain, R. K. *Nat. Rev. Cancer* **2003**, *3*, 380−387.

(7) Chatterjee, D. K.; Fong, L. S.; Zhang, Y. *Adv. Drug Delivery Rev.* **2008**, *60*, 1627−1637.

(8) Celli, J. P.; Spring, B. Q.; Rizvi, I.; Evans, C. L.; Samkoe, K. S.; Verma, S.; Pogue, B. W.; Hasan, T. *Chem. Rev.* **2010**, *110*, 2795−2838.

(9) Cheng, L.; Wang, C.; Feng, L.; Yang, K.; Liu, Z. *Chem. Rev.* **2014**, *114*, 10869−10939.

(10) Zhu, W.; Dong, Z.; Fu, T.; Liu, J.; Chen, Q.; Li, Y.; Zhu, R.; Xu, L.; Liu, Z. *Adv. Funct. Mater.* **2016**, *26*, 5490−5498.

(11) Idris, N. M.; Gnanasammandhan, M. K.; Zhang, J.; Ho, P. C.; Mahendran, R.; Zhang, Y. *Nat. Med.* **2012**, *18*, 1580−1585.

(12) Kotagiri, N.; Sudlow, G. P.; Akers, W. J.; Achilefu, S. *Nat. Nanotechnol.* **2015**, *10*, 370−379.

(13) Mitragotri, S. *Nat. Rev. Drug Discovery* **2005**, *4*, 255−260.

(14) Fan, C.-H.; Ting, C.-Y.; Lin, H.-J.; Wang, C.-H.; Liu, H.-L.; Yen, T.-C.; Yeh, C.-K. *Biomaterials* **2013**, *34*, 3706−3715.

(15) Ting, C.-Y.; Fan, C.-H.; Liu, H.-L.; Huang, C.-Y.; Hsieh, H.-Y.; Yen, T.-C.; Wei, K.-C.; Yeh, C.-K. *Biomaterials* **2012**, *33*, 704−712.

(16) McEwan, C.; Fowley, C.; Nomikou, N.; McCaughan, B.; McHale, A. P.; Callan, J. F. *Langmuir* **2014**, *30*, 14926−14930.

(17) Deepagan, V. G.; You, D. G.; Um, W.; Ko, H.; Kwon, S.; Choi, K. Y.; Yi, G.-R.; Lee, J. Y.; Lee, D. S.; Kim, K.; Kwon, I. C.; Park, J. H. *Nano Lett.* **2016**, *16*, 6257−6264.

(18) Ninomiya, K.; Ogino, C.; Oshima, S.; Sonoke, S.; Kuroda, S.-i.; Shimizu, N. *Ultrason. Sonochem.* **2012**, *19*, 607−614.

(19) Tachibana, K.; Feril, L. B.; Ikeda-Dantsuji, Y. *Ultrasonics* **2008**, *48*, 253−259.

(20) McEwan, C.; Owen, J.; Stride, E.; Fowley, C.; Nesbitt, H.; Cochrane, D.; Coussios, C. C.; Borden, M.; Nomikou, N.; McHale, A. P.; Callan, J. F. *J. Controlled Release* **2015**, *203*, 51−56.

(21) Umemura, S.; Kawabata, K.; Sasaki, K.; Yumita, N.; Umemura, K.; Nishigaki, R. *Ultrason. Sonochem.* **1996**, *3*, S187−S191.

(22) Yu, T. H.; Wang, Z. B.; Mason, T. J. *Ultrason. Sonochem.* **2004**, *11*, 95−103.

(23) Buettner, K. M.; Valentine, A. M. *Chem. Rev.* **2012**, *112*, 1863−1881.

(24) Rajh, T.; Dimitrijevic, N. M.; Bissonnette, M.; Koritarov, T.; Konda, V. *Chem. Rev.* **2014**, *114*, 10177−10216.

(25) Wang, L.; Sasaki, T. *Chem. Rev.* **2014**, *114*, 9455−9486.

(26) Lee, J. E.; Lee, N.; Kim, T.; Kim, J.; Hyeon, T. *Acc. Chem. Res.* **2011**, *44*, 893−902.

(27) Shi, J. L.; Chen, Y.; Chen, H. R. *Wuji Cailiao Xuebao* **2013**, *28*, 1−11.

(28) Lee, J. E.; Lee, N.; Kim, H.; Kim, J.; Choi, S. H.; Kim, J. H.; Kim, T.; Song, I. C.; Park, S. P.; Moon, W. K.; Hyeon, T. *J. Am. Chem. Soc.* **2010**, *132*, 552−557.

(29) Kim, J.; Kim, H. S.; Lee, N.; Kim, T.; Kim, H.; Yu, T.; Song, I. C.; Moon, W. K.; Hyeon, T. *Angew. Chem., Int. Ed.* **2008**, *47*, 8438−8441.

(30) Pan, L.; Liu, J.; Shi, J. *Adv. Funct. Mater.* **2014**, *24*, 7318−7327.

(31) Tu, H. L.; Lin, Y. S.; Lin, H. Y.; Hung, Y.; Lo, L. W.; Chen, Y. F.; Mou, C. Y. *Adv. Mater.* **2009**, *21*, 172−177.

(32) Chen, Y.; Meng, Q.; Wu, M.; Wang, S.; Xu, P.; Chen, H.; Li, Y.; Zhang, L.; Wang, L.; Shi, J. *J. Am. Chem. Soc.* **2014**, *136*, 16326−16334.

(33) Chen, Y.; Shi, J. *Adv. Mater.* **2016**, *28*, 3235−3272.

(34) Croissant, J.; Cattoen, X.; Man, M. W. C.; Gallud, A.; Raehm, L.; Trens, P.; Maynadier, M.; Durand, J.-O. *Adv. Mater.* **2014**, *26*, 6174−6180.

(35) Djojoputro, H.; Zhou, X. F.; Qiao, S. Z.; Wang, L. Z.; Yu, C. Z.; Lu, G. Q. *J. Am. Chem. Soc.* **2006**, *128*, 6320−6321.

(36) Teng, Z.; Wang, S.; Su, X.; Chen, G.; Liu, Y.; Luo, Z.; Luo, W.; Tang, Y.; Ju, H.; Zhao, D.; Lu, G. *Adv. Mater.* **2014**, *26*, 3741−3747.

(37) Li, X.; Zhou, L.; Wei, Y.; El-Toni, A. M.; Zhang, F.; Zhao, D. *J. Am. Chem. Soc.* **2014**, *136*, 15086−15092.

(38) Chen, Y.; Chen, H. R.; Shi, J. L. *Acc. Chem. Res.* **2014**, *47*, 125−137.

(39) Maggini, L.; Cabrera, I.; Ruiz-Carretero, A.; Prasetyanto, E. A.; Robinet, E.; De Cola, L. *Nanoscale* **2016**, *8*, 7240−7247.

(40) Chen, Y.; Chen, H.; Guo, L.; He, Q.; Chen, F.; Zhou, J.; Feng, J.; Shi, J. *ACS Nano* **2010**, *4*, 529−539.

(41) Chen, Y.; Chen, H. R.; Zeng, D. P.; Tian, Y. B.; Chen, F.; Feng, J. W.; Shi, J. L. *ACS Nano* **2010**, *4*, 6001−6013.

(42) Taylor, K. M. L.; Kim, J. S.; Rieter, W. J.; An, H.; Lin, W. L.; Lin, W. B. *J. Am. Chem. Soc.* **2008**, *130*, 2154−2155.

(43) Peng, Y.-K.; Lai, C.-W.; Liu, C.-L.; Chen, H.-C.; Hsiao, Y.-H.; Liu, W.-L.; Tang, K.-C.; Chi, Y.; Hsiao, J.-K.; Lim, K.-E.; Liao, H.-E.; Shyue, J.-J.; Chou, P.-T. *ACS Nano* **2011**, *5*, 4177−4187.

(44) Na, H. B.; Lee, J. H.; An, K. J.; Park, Y. I.; Park, M.; Lee, I. S.; Nam, D. H.; Kim, S. T.; Kim, S. H.; Kim, S. W.; Lim, K. H.; Kim, K. S.; Kim, S. O.; Hyeon, T. *Angew. Chem., Int. Ed.* **2007**, *46*, 5397−5401.

(45) Chen, Y.; Chen, H. R.; Zhang, S. J.; Chen, F.; Sun, S. K.; He, Q. J.; Ma, M.; Wang, X.; Wu, H. X.; Zhang, L. X.; Zhang, L. L.; Shi, J. L. *Biomaterials* **2012**, *33*, 2388−2398.

(46) Birnbaum, E. R.; Schaefer, W. P.; Labinger, J. A.; Bercaw, J. E.; Gray, H. B. *Inorg. Chem.* **1995**, *34*, 1751−1755.

(47) Angiolini, L.; Benelli, T.; Giorgini, L. *Polymer* **2011**, *52*, 2747−2756.

(48) Markovic, Z.; Todorovic-Markovic, B.; Kleut, D.; Nikolic, N.; Vranjes-Djuric, S.; Misirkic, M.; Vucicevic, L.; Janjetovic, K.; Isakovic, A.; Harhaji, L.; et al. *Biomaterials* **2007**, *28*, 5437−5448.

(49) Viswanathan, S.; Kovacs, Z.; Green, K. N.; Ratnakar, S. J.; Sherry, A. D. *Chem. Rev.* **2010**, *110*, 2960−3018.

(50) Caravan, P.; Ellison, J. J.; McMurry, T. J.; Lauffer, R. B. *Chem. Rev.* **1999**, *99*, 2293−2352.

(51) Kim, T.; Momin, E.; Choi, J.; Yuan, K.; Zaidi, H.; Kim, J.; Park, M.; Lee, N.; McMahon, M. T.; Quinones-Hinojosa, A.; Bulte, J. W. M.; Hyeon, T.; Gilad, A. A. *J. Am. Chem. Soc.* **2011**, *133*, 2955−2961.